AGU PUBLICATIONS

JGR

Journal of Geophysical Research: Oceans

RESEARCH ARTICLE

10.1002/2015JC011475

Downwelling wind, tides, and estuarine plume dynamics

Zhigang Lai[1,2], Ronghua Ma[1], Mingfen Huang[1], Changsheng Chen[3,4], Yong Chen[1], Congbin Xie[1], and Robert C. Beardsley[5]

[1]School of Marine Sciences, Sun Yat-Sen University, Guangzhou, China, [2]Key Laboratory of Marine Resources and Coastal Engineering in Guangdong Province, Guangzhou, China, [3]School for Marine Science and Technology, University of Massachusetts-Dartmouth, New Bedford, Massachusetts, USA, [4]International Center for Marine Studies, Shanghai Ocean University, Shanghai, China, [5]Department of Physical Oceanography, Woods Hole Oceanographic Institution, Woods Hole, Massachusetts, USA

Key Points:
- Wind and tide interactions are a dominant dynamics controlling the Pearl River plumes in the dry season
- Winds and tides can influence the plume dynamics both locally and remotely
- The wind-induced estuarine SSH is an indicator for the remote controlling mechanism of the plume dynamics

Correspondence to:
Z. Lai,
laizhig@mail.sysu.edu.cn

Citation:
Lai, Z., R. Ma, M. Huang, C. Chen, Y. Chen, C. Xie, and R. C. Beardsley (2016), Downwelling wind, tides, and estuarine plume dynamics, *J. Geophys. Res. Oceans*, *121*, 4245–4263, doi:10.1002/2015JC011475.

Received 14 NOV 2015
Accepted 9 MAY 2016
Accepted article online 12 MAY 2016
Published online 24 JUN 2016

Abstract The estuarine plume dynamics under a downwelling-favorable wind condition were examined in the windy dry season of the Pearl River Estuary (PRE) using the PRE primitive-equation Finite-Volume Community Ocean Model (FVCOM). The wind and tide-driven estuarine circulation had a significant influence on the plume dynamics on both local and remote scales. Specifically, the local effect of downwelling-favorable winds on the plume was similar to the theoretical descriptions of coastal plumes, narrowing the plume width, and setting up a vertically uniform downstream current at the plume edge. Tides tended to reduce these plume responses through local turbulent mixing and advection from upstream regions, resulting in an adjustment of the isohalines in the plume and a weakening of the vertically uniform downstream current. The remote effect of downwelling-favorable winds on the plume was due to the wind-induced estuarine sea surface height (SSH), which strengthened the estuarine circulation and enhanced the plume transport accordingly. Associated with these processes, tide-induced mixing tended to weaken the SSH gradient and thus the estuarine circulation over a remote influence scale. Overall, the typical features of downwelling-favorable wind-driven estuarine plumes revealed in this study enhanced our understanding of the estuarine plume dynamics under downwelling-favorable wind conditions.

1. Introduction

Freshwater runoff enters the sea and forms a coastal or estuarine type of river plume with distinct dynamics occurring mainly on the shelf or within the estuary. For coastal plumes, it is commonly recognized that winds are a dominant forcing driving the plume variability in regions where the tidal effects are ignorable [*Fong and Geyer*, 2001; *Garcia Berdeal et al*., 2002; *Lentz and Largier*, 2006]. However, this characterization of the plume dynamics may be problematic for estuarine areas where tides are usually important and the tidal and associated effects could be very influential in the plume even in regions dominated by winds [*Guo and Valle-Levinson*, 2007; *Yang and Khangaonkar*, 2009; *Hunter et al*., 2010]. Therefore, it is expected that the interaction of the river plume with both tides and winds is a general feature of estuarine plume dynamics.

Observational and theoretical studies show that downwelling- and upwelling-favorable winds in the coastal ocean could set up a dynamics with significantly different responses in the plume behaviors [*Chao*, 1988; *Münchow and Garvine*, 1993; *Fong et al*., 1997; *Chen et al*., 1999; *Whitney and Garvine*, 2005; *Choi and Wilkin*, 2007; *Jurisa and Chant*, 2012; *Pimenta and Kirwan*, 2014]. Generally, the downwelling wind stress causes a surface shoreward Ekman circulation to compress the plume against the coast. As a result, the plume exhibits an along-shore propagating feature of narrow width far from the source region [*Rennie et al*., 1999; *Moffat and Lentz*, 2012; *Mazzini et al*., 2014]. In contrast, the upwelling wind stress thins the plume by enhancing *its* offshore spreading [*Chen*, 2000; *Fong and Geyer*, 2001; *Lentz*, 2004]. This process continues under a persisting wind forcing until the strong mixing in the plume finally destroys it or the plume is eventually separated from the coast [*Chapman and Lentz*, 1994; *Fong and Geyer*, 2001; *Houghton et al*., 2004; *Hickey et al*., 2005].

For an estuarine plume influenced by wind, a downwelling-favorable condition is usually strongest during the winter when the freshwater discharge into the estuary is low and the wind is vigorous and persistent in

the seaward direction along the coast. Theoretically speaking, there are two physical processes which are fundamental in the downwelling-wind-forced plume dynamics under nontidal conditions [*Moffat and Lentz*, 2012]. One is the wind-induced deepening of the surface mixed layer, which entrains ambient water into the plume and steepens the isopycnals in the surface layer. The other is the steepening of the isopycnals in the plume due to the cross-shore Ekman transport, which narrows the plume width, changes the plume depth, and enhances the along-shore water transport.

Tidal and associated effects are potentially able to interact with the winds and cause a change in the estuarine plume dynamics. For example, tides enforce an energetic plume discharge. The resulting plume spreading may destroy the wind-induced surface mixed layer through tidal straining that tends to prevent it from being reestablished with enhanced vertical stratification [*Simpson et al*., 1990; *Hetland*, 2005]. Tides can precondition the vertical orientation of isopycnals in the plume through strong mixing [*MacCready and Geyer*, 2010]. This may ultimately change the timescale of cross-shore Ekman circulation in modifying the plume's structure and transport [*Whitney and Garvine*, 2005]. Since the estuarine stratification and mixing could also be controlled by wind-induced straining of the density field [*Scully et al*., 2005] and the tidally induced stratification and mixing has a varying strength during the flood-ebb tidal period and spring-neap cycles [*Li and Zhong*, 2009], the competition of tides with winds will have an effect on the spatial and temporal variability of the plume.

In many estuaries, the interaction of the river plume with tides and winds is fundamental in the estuarine subtidal dynamics. Generally, the subtidal dynamics in estuaries features a gravitational circulation that is due to the interplay of the plume induced horizontal salinity gradients and tides. This creates a two-layer flow with a surface seaward and bottom landward current under a forcing balance between the pressure gradient force and the tidally induced turbulent mixing [*Pritchard*, 1956; *Hansen and Rattray*, 1965]. The gravitational circulation in an estuary could be also influenced by the wind in two aspects. First, the wind can produce a similar two-layer flow with downwind current at surface and upwind current at depth, enhancing/reversing the gravitational circulation with a down-estuary/up-estuary wind stress [*Csanady*, 1973; *Winant*, 2004]. Second, the wind can cause a depth-independent change in the gravitational circulation by setting up a sea surface slope in the estuary, enhancing the barotropic volume exchange between the estuary and shelf [*Janzen and Wong*, 2002; *Pfeiffer-Herbert et al*., 2015]. It should be noted that these effects of wind forcing may vary widely due to the estuary's geometric scales and forcing characteristics. Their influences on the gravitational circulation have the potential to change the estuarine subtidal dynamics, which then modify the river plume in accordance [*Scully et al*., 2005]. Apparently, this effect of plume response is different from the local adjustment of the plume dynamics, as the former is determined by the wind forcing indirectly. This raises a question on whether or not a regional-scale (both local and remote) downwelling-favorable wind could influence or control the estuarine subtidal dynamics. In addition, it is clear that tide-induced strong turbulent mixing can influence the estuarine subtidal dynamics. However, whether and to what degree this would affect the remote controlling mechanism of the plume dynamics is still a question that deserves further investigation.

In this paper, a typical estuarine plume during the downwelling-favorable wind period was examined with an aim at understanding the dynamical processes described above. Unlike previous studies, this research is focused on the Pearl River Estuary (PRE), a mesotidal estuarine system located in the northern South China Sea (SCS) [*Mao et al*., 2004]. As shown in Figure 1, the PRE is about 70 km long and 25 km wide and has an average topographic depth of ~5 m. The prevailing climate in this area is controlled by the Eurasian monsoon [*Ding*, 1994], resulting in strong seasonal variability of freshwater runoff into the PRE. Typically, the Pearl River discharge during the dry season (October–May) is around 1500 m^3/s, but can increase up to 20,000 m^3/s during the wet season (April–September) [*Zhao*, 1990]. Affected by the monsoon climate, the wind is seasonally reversed over the coastal area. In the summer, the wind is predominantly southerly or southwesterly and has a magnitude of ~6 m/s; while in the winter, the wind is relatively stronger which is northerly or northeasterly and has a magnitude of ~8 m/s. During the winter dry season, the river discharge and wind forcing produce a typical downwelling-favorable wind-induced plume, which appears along the left (western) side of the estuary. More thorough study of plume dynamics here could enhance our understanding on downwelling-favorable wind-induced plumes in strong tidal environments that were not taken into account in previous modeling experiments.

Recently, a number of observational and numerical modeling studies have been conducted for the Pearl River plume in the dry season [*Dong et al*., 2004; *Wong et al*., 2004; *Ji et al*., 2011; *Zheng et al*., 2014; *Lai et al*., 2015].

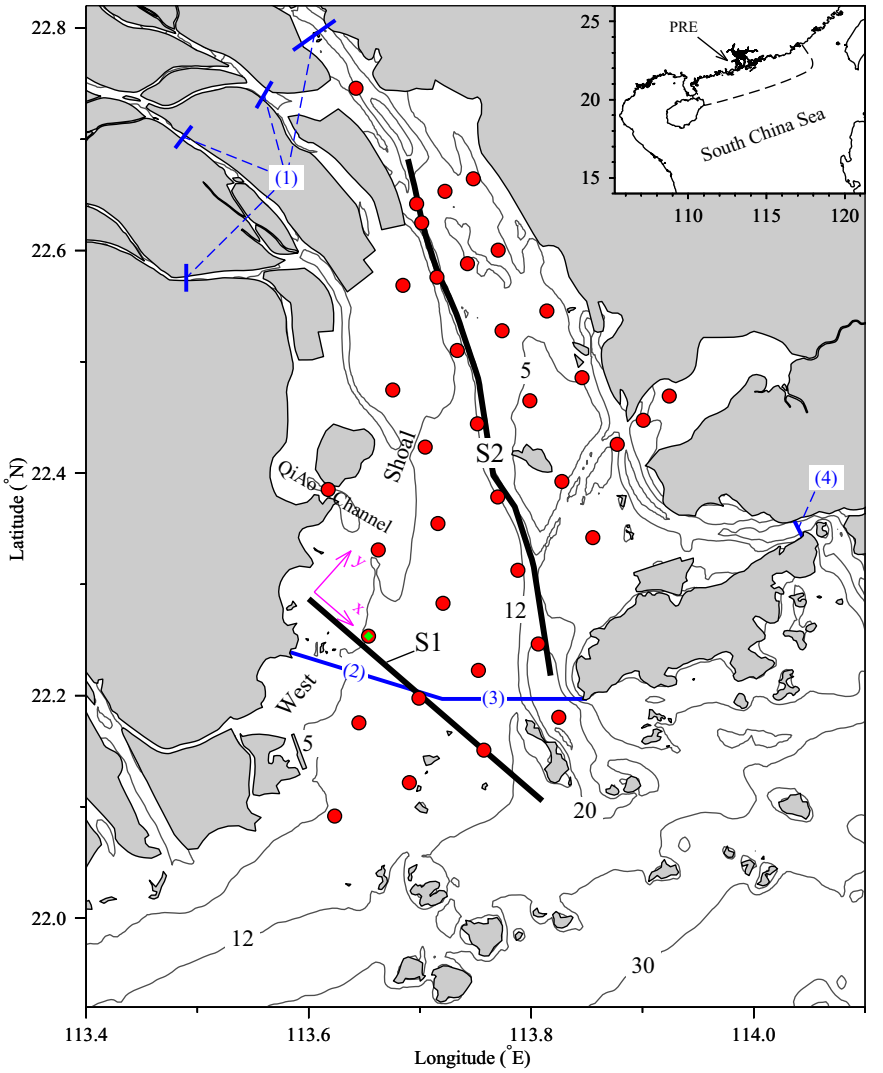

Figure 1. Enlarged view of the Pearl River estuary (PRE) with an indication of the location in the South China Sea and the model's open boundary (dash line) on the shelf. The red dots represent the locations where salinity data were collected. The green diamond represents the location where a momentum balance analysis was conducted. The sections used to close the estuary in the water budget estimation are indicated in solid blue lines labeled (1)–(4) as explained in the text. The black solid lines indicate the location of the cross-shore transect S1 and the along-shore transect S2, respectively. The local axes in magenta color indicate the positive value of the x (along-shore) and y (cross-shore) direction defined in Figures 9 and 12.

Based on the results, it is clear that the wind forcing has a major influence on the plume with a time scale longer than the tidal periods. However, little research has been conducted to examine the plume dynamics under the wind's influence in detail. To address this question, it is necessary to establish a high-resolution 3-D circulation model that is capable of resolving the complex estuarine environment in the PRE with realistic geometry and forcing conditions. Recently, we have developed such a model and successfully used it to understand the impact of the multichannel river network on the plume dynamics in the dry season [*Lai et al*., 2015]. This model allows us to investigate the downwelling-favorable wind-induced plume dynamics in the PRE, particularly on addressing questions related with saltwater intrusion, water quality, and ecosystem function and health in the dry season [*Dai et al*., 2006; *Qiu et al*., 2010; *Gong and Shen*, 2011; *Zhang et al*., 2012].

The remainder of this paper is organized as follows. In section 2, the model setup, forcing conditions, and model validation are described. In section 3, the major findings of the plume structure and dynamics associated with tides and winds are presented, followed by a detailed discussion in section 4. Finally, the conclusions are summarized in section 5.

2. Model Setup and Validation

2.1. Model Setup

The numerical study was based on the Pearl River Estuary 3-D primitive equation, Finite-Volume Community Ocean Model (PRE-FVCOM) [*Lai et al*., 2015]. FVCOM was originally developed by *Chen et al*. [2003] and has been continuously improved and updated by the joint research team of University of Massachusetts-Dartmouth and Woods Hole Oceanographic Institution [*Chen et al*., 2006a, 2006b, 2013]. The PRE-FVCOM was configured in the manner as described by *Lai et al*. [2015], in which several key features were designed that makes the model particularly suited for the simulation of the Pearl River plume in the dry season. First, the model has a large computational domain that not only extends to the shelf of the northern SCS along the 100 m isobath but also covers the entire Pearl River network by setting the river boundary at the upstream limit of tidal influence. With this, it is capable of resolving the interaction of the river network and the estuary, a key aspect of the plume dynamics in the dry season [*Lai et al*., 2015]. Second, PRE-FVCOM has an unstructured horizontal grid with a resolution varying from $\sim$10 km at the open boundary down to $\sim$20–300 m within the Pearl River. Geometric flexibility in the grid configuration provides a realistic and accurate representation of the complex coastline and islands in the PRE. Vertically, the model has 45 layers configured with a hybrid terrain-following coordinate, using the s-coordinate transformation in water depth $>$ 225 m and the σ-coordinate in water depth $\leq$ 225 m. The transition between the two coordinates is at the 225 isobath where all layers have a uniform thickness of 5 m. The s-coordinate is configured with a depth-independent uniform layer thickness in the upper water column and over the bottom slope in the continental shelf, which are critically important to resolve the wind-induced surface mixed layer and tidal-induced sloping bottom boundary layer [*Chen et al*., 2016]. The σ-coordinate used in the model ensures that the vertical circulation can be resolved well enough in this shallow estuary where the tidal range is $\sim$2 m and the undistributed mean water depth is $\sim$5 m [*Lai et al*., 2015]. In addition, the combination of the PRE-FVCOM horizontal and vertical spatial resolution is such that the transport through the QiAo Channel (Figure 1) could be simulated correctly in order to capture the plume structure and dynamics over the West Shoal [*Lai et al*., 2015]. Third, the model is driven under realistic forcing conditions that include well-calibrated tidal elevations at the open boundary, observed river discharge at upstream hydrological stations and predicted surface forcing from a 4 $\times$ 4 km resolution WRF (Weather Research and Forecast) community mesoscale weather model. This is important because it not only allows a more straightforward model-data comparison but also drives a highly accurate plume field, which is a prerequisite for the following analysis of the dynamics.

Finally, it is worth noting that the simulation was conducted with both spatially varying temperature and salinity (T/S) fields, even though temperature has less contribution to the density of the PRE. To set up the temperature and salinity simulation, an initial climatology of the T/S field was specified in the model. In addition, a proper tracer radiation condition was set at the open boundaries. For the tracer condition at the river boundaries, we simply set the salinity to be 0 and the temperature to be a constant value that varies seasonally. Having been described thoroughly, these and other details on the model setup can be found in *Lai et al*. [2015].

2.2. Forcing Conditions

The numerical model simulation was chosen for a period from 1 November to 31 December 2006, during which the observations obtained from a field survey conducted on 20–21 December 2006 were available for model-data comparisons. A total of 37 CTD stations were sampled at the locations indicated in Figure 1 during spring tidal period [*Liu et al*., 2006]. This data set has a good spatial coverage over the PRE with a high sampling resolution, which is particularly useful to validate the model-predicted plume structure.

The time series of the total Pearl River discharge during the model simulation period had a peak around 22 November 2006 (Figure 2). After that, the discharge gradually decreased and remained stable at a mean level of $\sim$3000 m^3/s over December 2006. Since the river discharge that enters the PRE was roughly half of the total Pearl River discharge, the model-predicted plume exhibited a size comparable to the climatological mean with small fluctuations caused by the variations of the total river discharge.

Wind plays a critical role in the successful simulation of the wind-forced plume dynamics. For this study, three wind time series were generated (Figures 3a–3c, left). First, the measured hourly wind at Hong Kong airport was chosen to represent the wind field over the PRE (hereafter referred to as Wind HK). Second, the

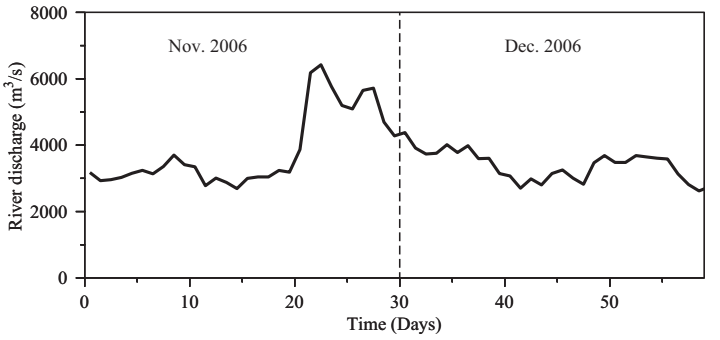

Figure 2. Time series of the hourly total Pearl River discharge during the model simulation period.

output from a 4 × 4 km resolution north SCS WRF model (hereafter referred to as Wind WRF) was used. Third, the north SCS WRF was rerun with assimilation of the measured hourly wind at the three airports around the PRE (hereafter referred to as Wind WRF-assim). To view the differences among the three wind time series, one can examine the left plot in Figure 3. Generally, the time series of Wind HK showed a relatively smaller magnitude in wind speed and a larger variation in wind direction. This is contrary to the Wind WRF time series, which showed a relatively larger magnitude in wind speed and a smaller variation in wind direction. In contrast, the Wind WRF-assim looked more like a combination of the Wind HK and the Wind WRF. To compare the three winds more clearly, the monthly mean wind field over the PRE is shown in the right plot of Figure 3. Consistent with the time series data, the Wind WRF-assim had a magnitude that was stronger than the Wind HK but weaker than the Wind WRF. However, all winds had a similar direction, which is northeasterly, even though they exhibited a different degree of variation (Figure 3, right). In order to determine which wind forcing is the best for the following analysis, numerical experiments were designed to examine the simulated plume under the three winds by comparing with the observations, respectively. For the purpose of analysis, two additional numerical experiments were conducted. Specifically, one experiment aimed to examine the plume dynamics without the wind effect (referred as "with no-wind"). The other experiment aimed to examine the plume dynamics without the effect of tides (referred as "with no-tide"). In the latter case, the wind forcing was the same as that used in the Wind WRF-assim case.

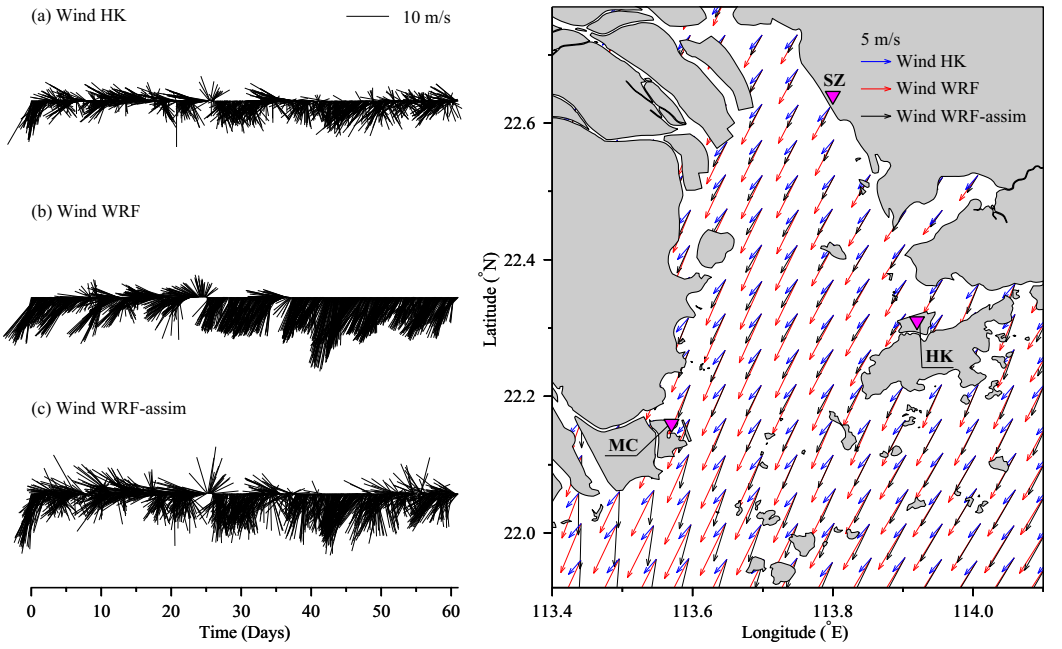

Figure 3. (left) Time series of the single point wind speed and direction (location: 113.75°E, 22.35°N) in the case of Wind HK, Wind WRF, and Wind WRF-assim, respectively during the GMT time from 1 November to 31 December 2006. (right) The monthly mean wind field in the case of Wind HK, Wind WRF, and Wind WRF-assim, respectively. The locations of the airports in Shen Zhen (SZ), Hong Kong (HK), and Macau (MC) surrounding the PRE are indicated. The hourly wind data collected from these airports' weather stations were used for the data assimilation in the WRF model.

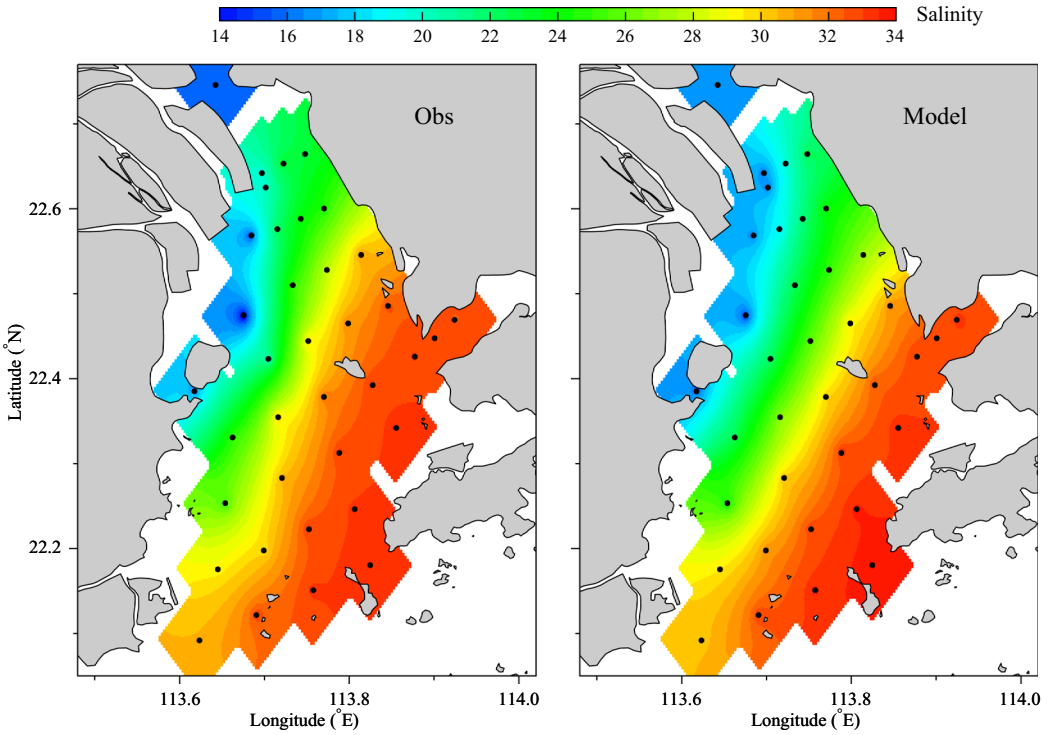

Figure 4. Model-data comparison of the surface salinity field predicted in the case of Wind WRF-assim. (Since density in the PRE region is dominated by salinity, we plot only salinity in this and following figures.)

2.3. Model Validation

The model-predicted values of salinity were output at the same locations and times where and when the observations were made, and the model-data comparison was made on the observed surface plume. Taking the Wind WRF-assim case as an example, the model results matched the observations very well in both the salinity values and the spatial distribution (Figure 4). Specifically, the observations showed a clear pattern of salinity contours roughly in the northeast-southwest orientation, with low-salinity water (<20) located at the estuary head and the northwest corner around the mouths of river outlets and high-salinity water (>32) intruding toward the northeast from the shelf. The model-simulated salinity field resembled that to a large degree, except that the area of low-salinity water at the head of the estuary was relatively larger. The model pushed the local salinity contours farther offshore in the southeast direction.

To quantify the accuracy of the model results, three parameters were calculated: the root-mean-square (RMS) error, the correlation coefficient (CC), and a non-dimensional skill assessment parameter defined in *Warner et al.* [2005] and used by *Pan et al.* [2014] to validate their model results in the PRE. The skill parameter is given as

$$Skill = 1 - \frac{\sum_{i=1}^{N} (s_{mo} - s_{ob})^2}{\sum_{i=1}^{N} (|s_{mo} - \bar{s}_{ob}| + |s_{ob} - \bar{s}_{ob}|)^2} \quad (1)$$

where s_{mo} and s_{ob} represent the model and observed salinity, respectively, the overbar means averaging over the data set, and N is the number of observations.

To assess the accuracy of the three wind fields used in the plume simulations, the same model-data comparisons for the Wind HK, Wind WRF, and WRF-assim cases are plotted in Figure 5. The results showed that with a stronger magnitude of wind, the model with Wind WRF overestimated the surface salinity values or alternatively underestimated the plume, while the model with Wind HK underestimated the salinity values and overestimated the plume. The model with Wind WRF-assim produced the best model-data comparison.

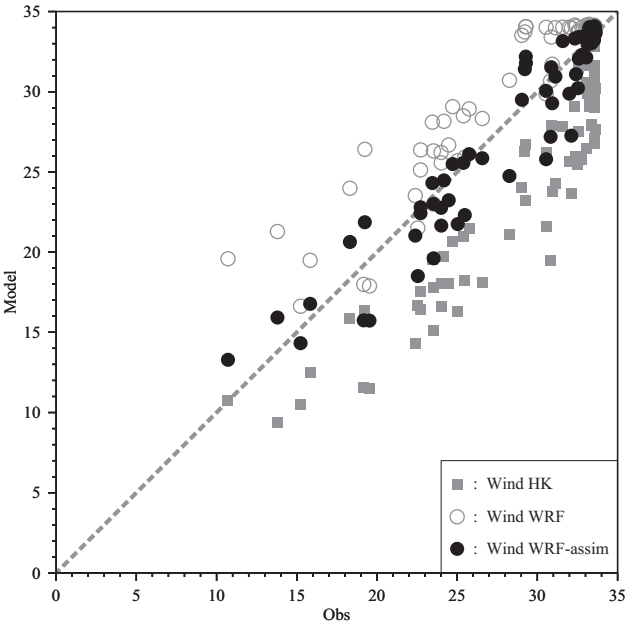

Figure 5. Model-data comparison of surface and subsurface salinity in the case of Wind HK, Wind WRF, and Wind WRF-assim, respectively.

This conclusion was also confirmed by the statistical error analysis. While the results shown in Table 1 indicated that although all wind fields could produce a plume with a structure similar to the observed salinities, the size of the plume was very sensitive to the magnitude of the wind. The model-predicted plume forced by the Wind WRF-assim field was optimal, with a model skill parameter of 0.98, very close to perfect skill (a value of 1).

3. Results

3.1. Plume Geometry

The detided mean geometry of the model-predicted plume was examined over the period December 2006. The subtidal feature of the plume was obtained by removing the diurnal and higher-frequency tidal signals using a 33 h low-passed filter (named PL64TAP) [*Beardsley and Rosenfeld*, 1983]. Alternatively, one could choose a more thorough way by subtracting tides from the hourly time series using T_Tide [*Pawlowicz et al*., 2002]. Since no significant difference was found using these two methods, we present the 33 h low-passed filter results.

The mean surface plumes for the cases with (a) no-wind, (b) Wind HK, (c) Wind WRF-assim, and (d) Wind WRF are shown in Figure 6. The results show that winds cause a significant reduction of the plume's lateral scale. The downwelling-favorable winds play a dominant role in determining the plume's subtidal structure even under relatively strong tidal conditions. In addition, comparing the plume width as a function of wind speed (Figure 3) indicated that the lateral scale of the plume was reduced significantly during a certain range of the wind speed increase and then converged toward a more stable scale as the wind continuously intensified. This suggests that the effect of the downwelling-favorable winds on the plume width may have an upper cap if the wind strength exceeds a certain threshold.

To quantify the subsurface response of the plume under a downwelling-favorable wind forcing, we examined the plume's vertical structure on the transect S1. Based on Figures 6c and 6d, the plume with downwelling-favorable winds only appeared along the west PRE with the spatial distribution parallel to local isobaths and converged toward the west as the wind increased. Therefore, transect 1 is a cross-estuary section, running from the west coast to the mouth of the estuary. Although this section was not long enough to cover the entire structure of the plume under the no wind condition, it showed little influence on the analysis results presented in the following discussion. In the following analyses of the effects of tides in the plume dynamics, the results of the Wind HK case were replaced by the results of the no-tide case, since the formal can be interpreted based on the results from the no-wind and the Wind WRF-assim cases.

The mean salinity distribution along the transect S1 is shown in Figure 7 for the four cases described above. Consistent with the change of the plume's surface expression, the downwelling-favorable wind-induced cross-shore Ekman circulation caused a substantial adjustment of the plume's lateral scale at depth. For example, without wind forcing the plume could expand over the continental slope, with top-to-bottom isohalines sloping in the offshore direction. In the three cases with wind forcing, the plume was confined on the shelf with the isohalines being nearly vertical. This large contrast in the plume's vertical structure was reported in previous studies, which was associated with the plume's initial

Table 1. The Model-Data Statistical Parameters for the Simulations Driven by the Wind HK, Wind WRF, and Wind WRF-assim Wind Fields

Case	RMS	CC	Skill
Wind HK	5.3	0.93	0.84
Wind WRF-assim	1.8	0.96	0.98
Wind WRF	2.7	0.94	0.94

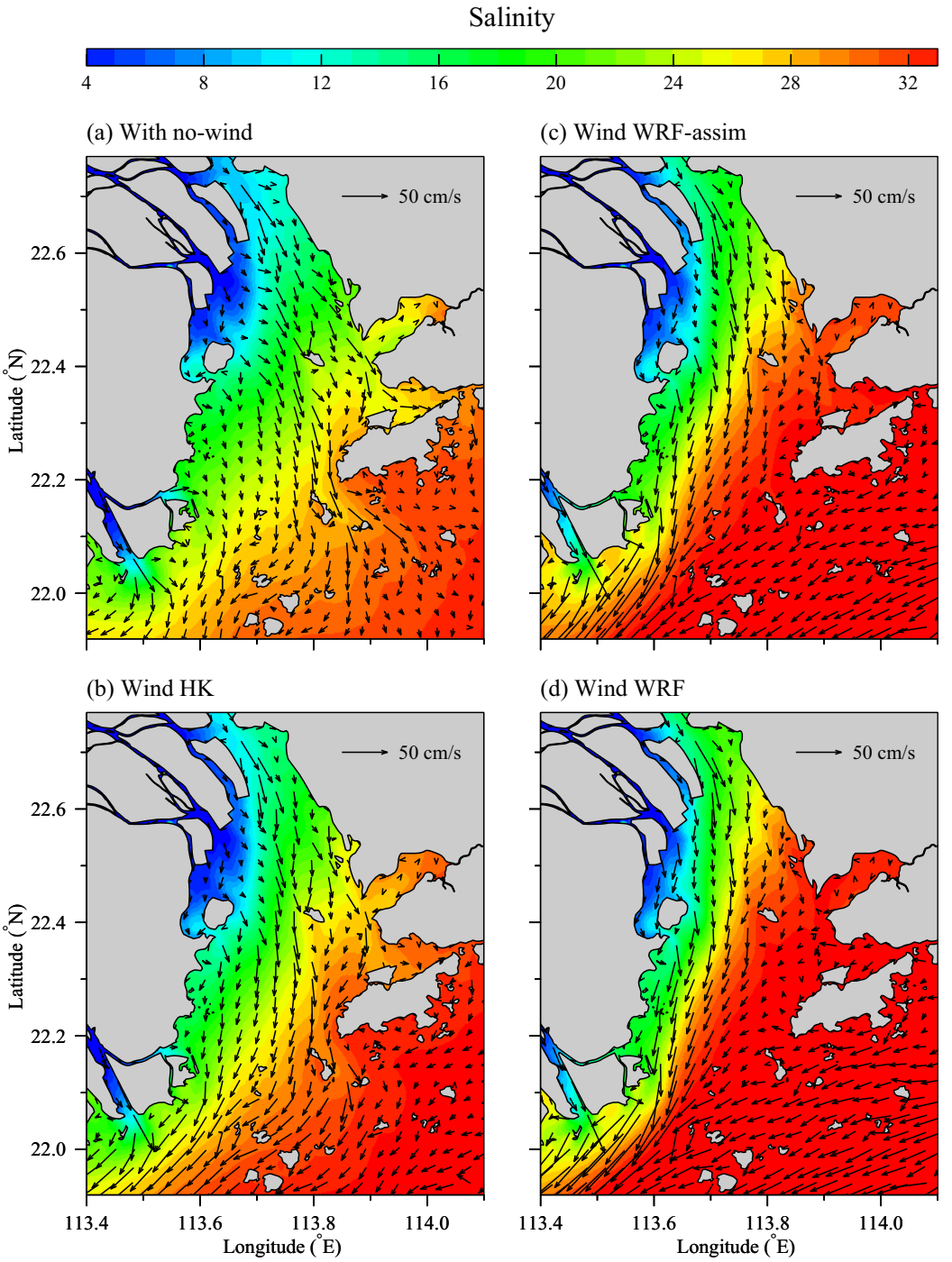

Figure 6. Model-predicted mean surface salinity and current in the case (a) with no-wind, (b) the Wind HK case, (c) the Wind WRF-assim case, and (d) the Wind WRF case, respectively.

geometry at the start of wind blowing under a nontidal condition [*Moffat and Lentz*, 2012]. This should also be valid in the current study under tidal and varying wind environments. In addition, the results in Figure 7 suggest a secondary role of tides on the plume's subtidal structure since the salinity distributions in the case with no-tide and the Wind WRF-assim case looked very similar.

To qualify the effect of tides on the plume's geometry, we next examined the salinity difference on the transect S1 for the cases with no-wind, no-tide, and Wind WRF, respectively, relative to the Wind WRF-assim

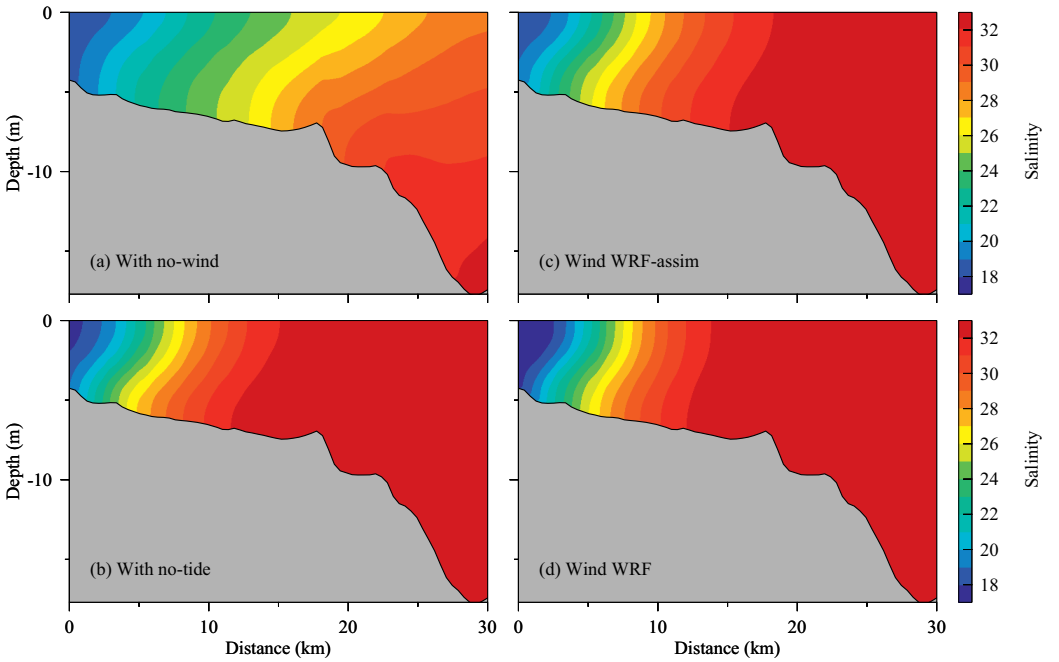

Figure 7. Model predicted mean salinity distributions along section S1 in the (a) case with no-wind, (b) case with no-tide, (c) the Wind WRF-assim case, and (d) the Wind WRF case, respectively.

case (Figure 8). In the no-wind case, the offshore spreading of the plume caused a large area of negative salinity difference. While both in the no-tide and the Wind WRF cases, it showed a positive salinity difference in the river plume except in the nearshore region. A further comparison showed that the detailed pattern of the salinity difference in the no-tide and Wind WRF cases was distinct. For example, in the no-tide case, there was a bottom area of large salinity difference which was suspected to be associated with the tidally induced strong turbulent mixing in the bottom boundary layer. In addition, the salinity difference in the no-tide case tended to be strong at surface and bottom with a minimum located in the middepth, suggesting that tides had an effect to adjust the vertical orientation of the isohalines in the plume. In contrast, however, the maximum of the salinity difference in the Wind WRF case was only located at the surface, which was consistent with the surface Ekman dynamics as a stronger wind stress could cause an enhanced surface turbulent mixing. Finally, in both the no-tide and Wind WRF cases, the maximum salinity difference tended to be centered at a distance about 10–11 km along the profile. We will return to this point in the following analysis.

3.2. Plume Current

The model-predicted mean currents on the transect S1 for the four cases are shown in Figure 9. In contrast, the plume with no wind featured a two-layer flow with offshore/onshore current in the cross-shore direction and downstream/upstream current in the along-shore direction. Downwelling-favorable wind enhanced the two-layer flow in both the cross-shore and along-shore directions and intensified the flow in the surface layer. Comparing the results for the cases with (a) no-wind and (c) Wind WRF-assim suggested that the near-surface flow intensification was most obvious in the along-shore direction, resulting in a vertically uniform downstream current that first appeared at the shelf-break and then expanded in width with the increase in wind speed. In all wind-forcing cases, there existed a cross-shore flow convergence on the offshore side of the vertically uniform downstream current. This was also evident in Figure 6, marking the boundary between the near-shore plume water and the offshore shelf water.

The tidal effects on the current structure of the plume are evident in Figure 9 by comparing the cases with (b) no-tide and (c) Wind WRF-assim. With the inclusion of tides, the two-layer flow in the cross-shore and along-shore directions became relatively weaker. In addition, tides significantly weakened the vertically uniform downstream current. It seems to be counter to our understanding on the role of tides in the plume, which was expected to increase vertical mixing and overcome the upstream buoyancy input. A possible

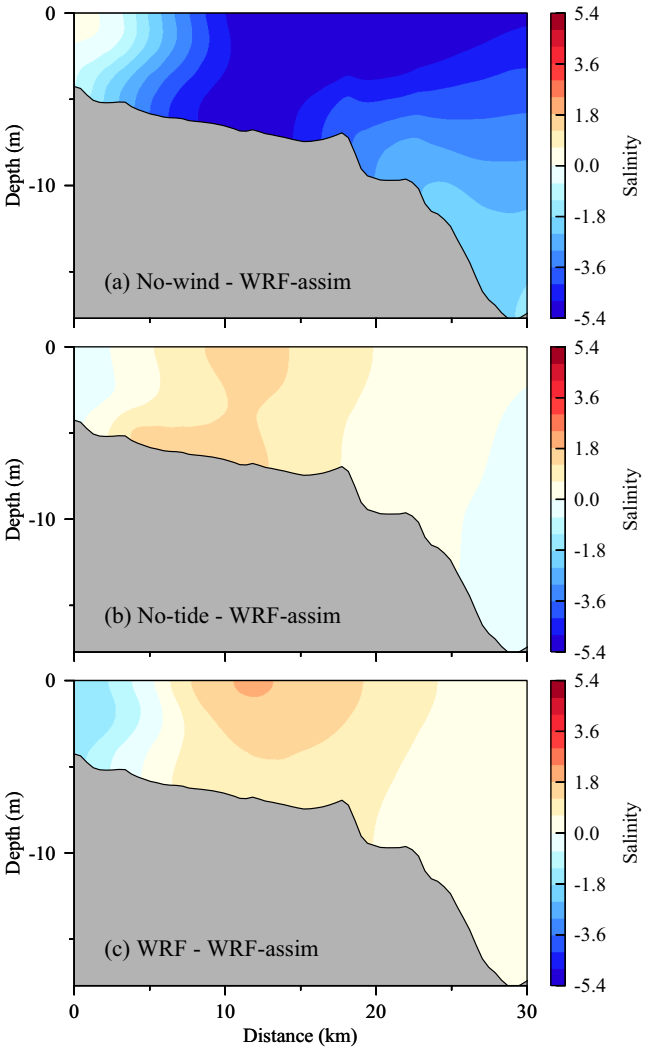

Figure 8. Salinity difference in the (a) with no-wind, (b) with no-tide, and (c) Wind WRF cases, respectively, relative to the Wind WRF-assim case along section S1.

reason was that the tidally enhanced upstream buoyancy input suppressed the local wind-induced turbulent mixing in the near-shore area. Thus, the competition of these two processes caused the different dynamics in the inshore and offshore areas of the plume.

To verify the competition effect of tidal and wind processes on the vertical mixing which results in an adjustment of the current structure of the plume, we calculated the model-predicted Richardson number at a location of 5 km where the two-layer flow always existed and at a location of 17 km where the two-layer flow disappeared in Figures 9c and 9d over December 2006 (Figure 10). The Richardson number was defined as $Ri = -\frac{g}{\rho_o}\frac{\Delta\rho}{(\Delta u)^2}$ where g was gravity, ρ_o was the reference density, and $\Delta\rho$ and Δu were the vertical density and current differences between two grid layers, respectively. The resulting Ri was divided by 0.25 and transformed using the logarithm function with a base of 10. The regions with negative values indicated a dominance of vertical mixing over buoyancy input while the regions with positive values indicated a suppression of vertical mixing by buoyancy input. In both (c) Wind WRF-assim and (d) Wind WRF cases, the nearshore region was dominated by the process of buoyancy input which prevented mixing through wind stirring. In the offshore region, this relationship was reversed frequently due to the strengthening of wind forcing.

Finally, the comparison between Figures 9b and 9c suggested that the increased downstream plume water transport in the no-tide case should not be purely the effects of local tidal mixing or upstream buoyancy input. Based on the plume theory, the wind-driven circulation only induces a change of vertical velocity profile without incurring any net water transport. This means that other effect of tides could be involved in the downwelling wind-forced plume dynamics.

3.3. Plume Front

The plume featured a density front which could be influenced by the downwelling-favorable wind. In Figure 11, the surface and bottom salinity gradients on the transect S1 were estimated to define the fronts based on the salinity distributions displayed in Figure 7. The results showed that, in all cases, the front position remained unchanged, with the surface front located at $x = \sim$6 km and the bottom one located at $x = \sim$4 km, about 2 km closer to the coast.

The momentum balance analysis (shown in Figure 12) was conducted at a location of the front (Figure 1) to examine the underling dynamics that led to the model predicted frontal structure. With no-wind, the cross-shore momentum was fundamentally geostrophic with a barotropic pressure gradient force balanced by

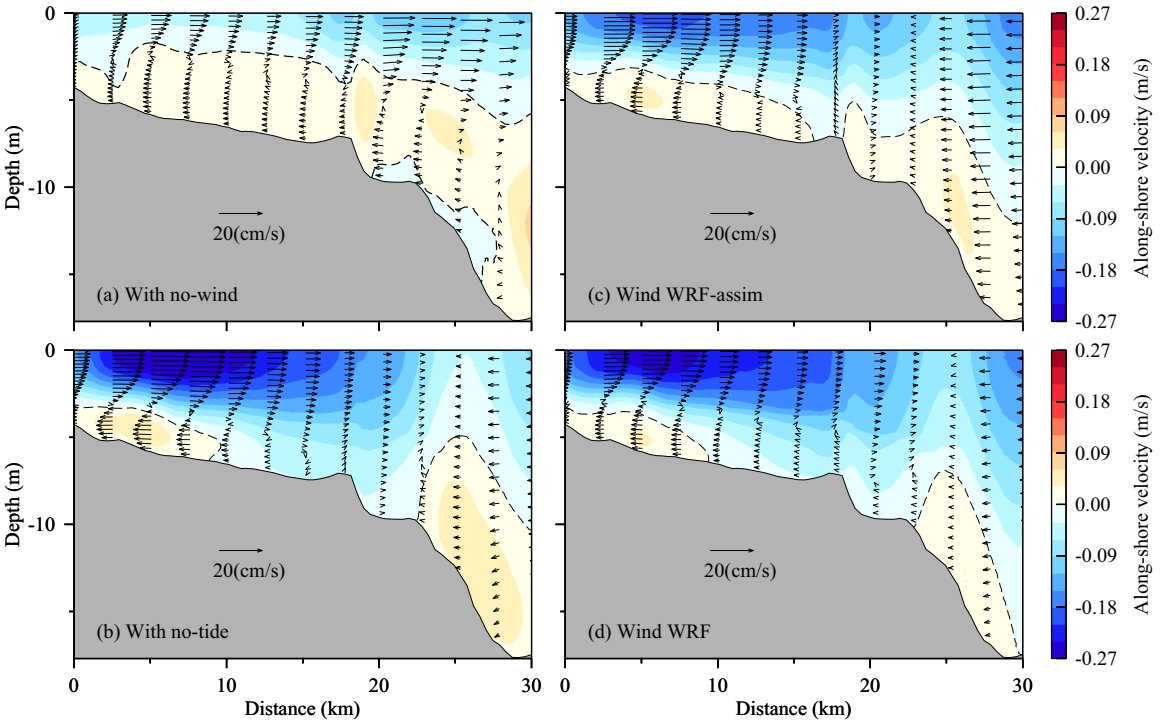

Figure 9. Model predicted mean current along section S1 in the (a) with no-wind, (b) with no-tide, (c) Wind WRF-assim, and (d) Wind WRF cases, respectively. The vectors represent the cross-shore current while the color image represents the along-shore current with the downstream current indicated by negative values and vice versa.

the Coriolis force at the surface. The baroclinic pressure gradient force increased with depth, which was balanced by the barotropic pressure gradient force, the Coriolis force, and the bottom friction at the bottom. Turning on the wind forcing did not change the dominant cross-shore momentum balance. The only difference is that the wind enhanced the vertical diffusion term. In this case, a much stronger barotropic pressure gradient force was required to act against the surface wind drag force and to balance the baroclinic pressure gradient force at depth. Apparently, the results suggest that although the downwelling-favorable winds cause a significant adjustment of the cross-shore barotropic/baroclinic pressure gradients, their effects on the momentum balance are largely canceled out by each other. Therefore, the cross-shore plume dynamics should be under a geostrophic balance with an offshore distance of the front determined by the internal Rossby radius of deformation [*Lentz and Larger*, 2006].

The internal Rossby radius of deformation is defined here as $R=\frac{\sqrt{g'H_o}}{f}$ where H_o is plume thickness, f is the Coriolis parameter and $g'=g\frac{\Delta\rho}{\rho_o}$ given the gravity g, the reference density ρ_o and the fluids' density difference $\Delta\rho$ between the distance at the coast and the front. The characteristic values used in the estimation were $H_o=6$ m, $f=5.5316\times10^{-5}$ 1/s and the surface $\Delta\rho=$ 1.8, 4.4, 4.3, and 5.9 kg/m^3 for the cases with (a) no-wind, (b) no-tide, (c) Wind WRF-assim, and (d) Wind WRF, respectively. The resulting R was 5.9, 9.2, 9.1, and 10.6 km for the four cases. It was clear that the estimated R could match the offshore distance of the surface front only in the case with no-wind. In all other cases with wind forcing, R was much larger than the model-predicted values. Again, this result confirms that the downwelling-favorable winds are not able to change the location of the front which has an offshore distance determined by R under the no-wind condition.

This result may also explain why the strong cross-shore salinity difference in Figure 8 tended to be centered at a location about 10–11 km offshore. This suggests that the cross-shore plume dynamics is different on the inshore and offshore sides of the front. Specifically, the cross-shore Ekman dynamics is effective at the offshore side of the front where the plume's lateral scale is compressed and cross-shore salinity gradients are larger. On the inshore side of the front, the wind effects on the cross-shore momentum balance are canceled out by each other and the plume remains geostrophic in the cross-shore direction.

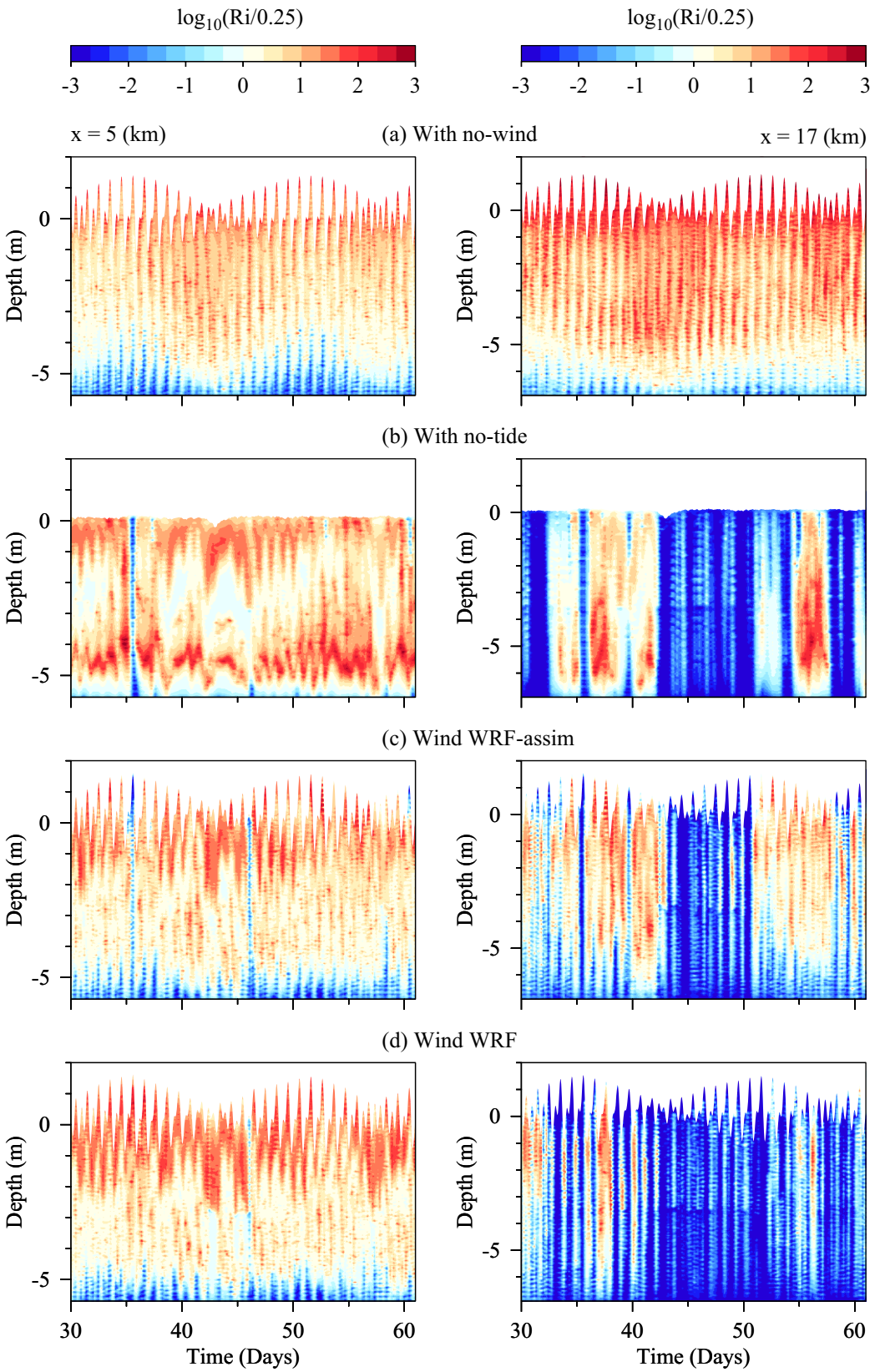

Figure 10. Time series of the calculated $\log_{10}(R_i/0.25)$ at the location of 5 km and 7 km along section S1 in the (a) with no-wind, (b) with no-tide, (c) the Wind WRF-assim, and (d) Wind WRF cases, respectively. The definition of the Richardson number is explained in the text.

Previous studies revealed that buoyant coastal plumes over the continental shelf were dynamically under a semigeostrophic balance with an along-shore current profile following the thermal wind relationship [*Blanton*, 1981; *Garvine*, 2004; *Lentz and Largier*, 2006]. For the plume in the PRE, we did not find this feature. Our results suggested that based on the along-shore momentum balance, the plumes had a significant longitudinal acceleration under both tidal and wind conditions (Figure 12, right), so that the plume theory based on simple linear dynamics was not applicable.

3.4. Plume Transport

The investigation of the current structure in Figure 9 suggested that the increased plume transport in the case with no-tide should not be purely due to a local adjustment of plume dynamics. To understand the associated dynamics, the connection of the plume transport with the freshwater input and the estuary-shelf exchange was examined to see whether it was associated with the estuarine circulation. In order to do that, the PRE was treated as a closed body of water by defining sections at the river outlets, the estuary mouth, and the deep channel between Hong Kong Island and the mainland of the delta (Figure 1). The mean subtidal transport through these sections was calculated by filtering the hourly model output and averaging the time series over the period of December 2006. This method was the same as described in *Lai et al*. [2015]. For the ease of analysis, the transports through the four river outlets were summed up and labeled as "(1)" which collectively represented the freshwater input from the Pearl River, while the transport through the estuary mouth needed to be divided into two parts which roughly separated the section of plume transport "(2)" from the estuary-shelf exchange "(3)" in the rest of the section. Finally, the transport through the channel between the Hong Kong Island and the mainland of the delta was labeled as "(4)."

The results (displayed in Figure 13) showed that with a same freshwater input from the river, the water budget in the estuary determined the plume transport at the estuary mouth was exactly balanced by the estuary-shelf exchange with a pattern completely different for the cases with/without the effects of wind. Specifically, the removal of the wind forcing caused the plume water to be transported out of the estuary mainly through the sections (3) and (4) while the transport at section (2) was directed upstream as compensation. These results were consistent with the corresponding features of the plume at the surface (Figure 6a) and in the cross-shore section (Figure 9a). In contrast, when the wind forcing was turned on, such a clockwise pattern of the estuarine water transport was reversed. It was characterized by a strong plume transport out of the estuary at section (2) and enhanced water exchange into the estuary at sections (3) and (4). This finding suggests that for a downwelling wind-forced estuarine plume, the increased water transport in the plume might not fully be the results of the local adjustment of the dynamics and that the wind-induced estuary-shelf exchange could be important too. In addition, the results showed a consistently enhanced transport at sections (2)–(4) in the case with no-tide comparing with the Wind WRF-assim case. This confirms that tides should also be involved in the process of the estuary-shelf exchange to provide a remote mechanism on the plume dynamics.

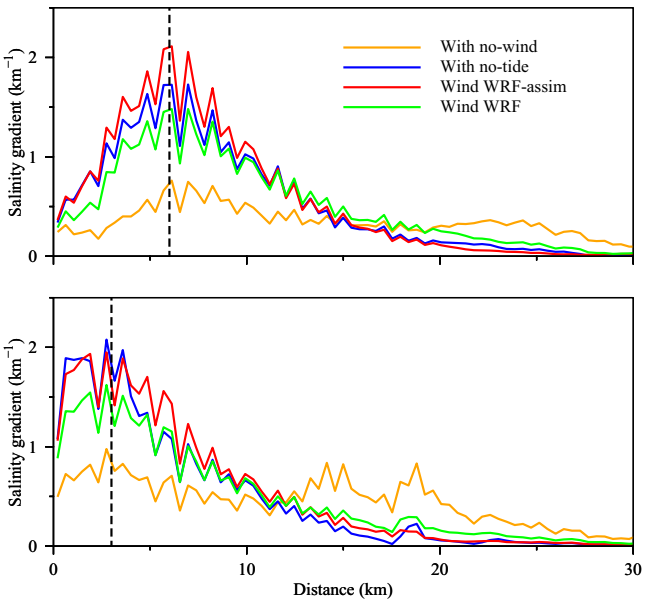

Figure 11. Calculated surface and bottom salinity gradient along section S1 in the (a) with no-wind, (b) with no-tide, (c) Wind WRF-assim, and (d) Wind WRF cases, respectively.

4. Discussion

Previous studies of the downwelling wind-forced plumes were focused on the local processes of wind influences. Our numerical model study of the PRE plume suggests that the regional-scale downwelling-favorable wind could also have a remote influence on the

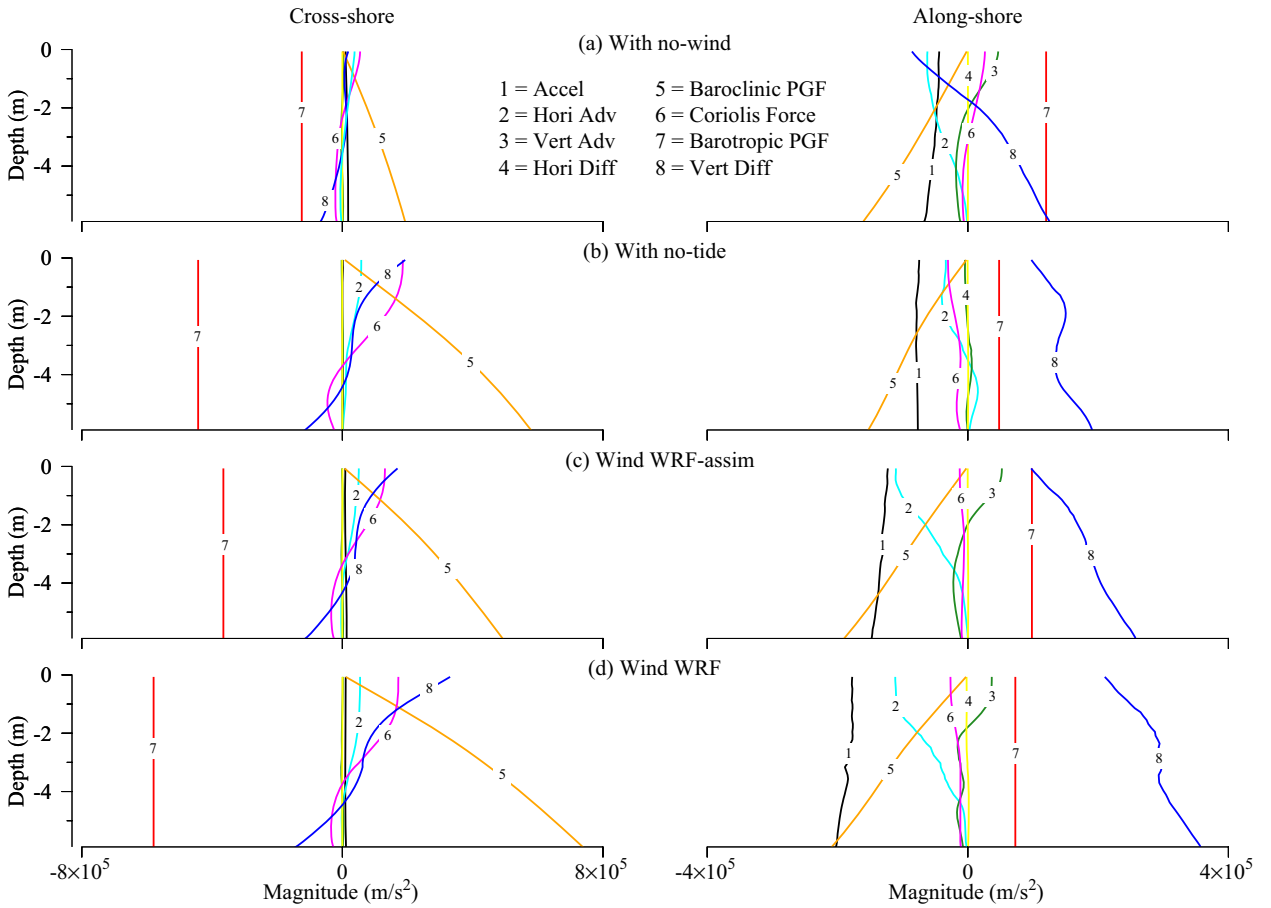

Figure 12. Monthly mean along-shore and cross-shore momentum balance in the (a) with no-wind, (b) with no-tide, (c) Wind WRF-assim, and (d) Wind WRF cases, respectively, at the location indicated in Figure 1.

estuarine plume dynamics. By analyzing the water budget in the PRE, it is clear that this remote mechanism is associated with the wind-driven estuarine circulation, which enhances the plume transport through an active estuary-shelf exchange.

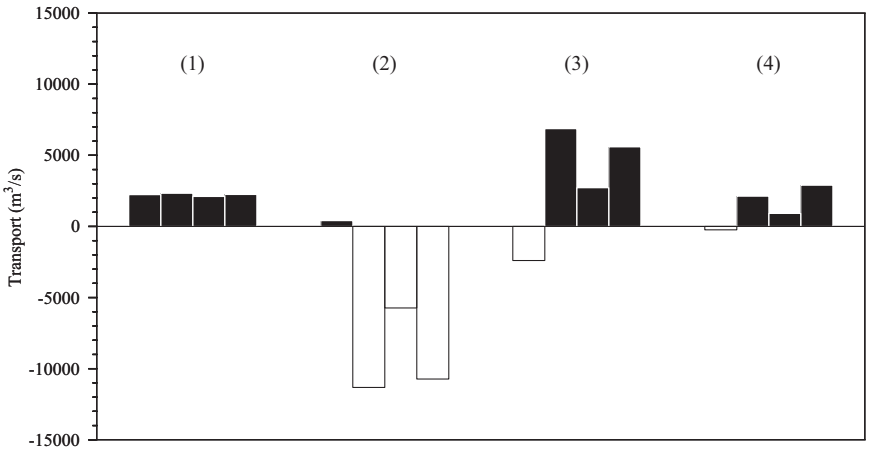

Figure 13. Transport at section (1)–(4). The transport in the (a) with no-wind, (b) with no-tide, (c) Wind WRF-assim, and (d) Wind WRF cases, respectively, is arranged at each section in an order from left to right. The positive value means the net transport is directed into the estuary and vice versa.

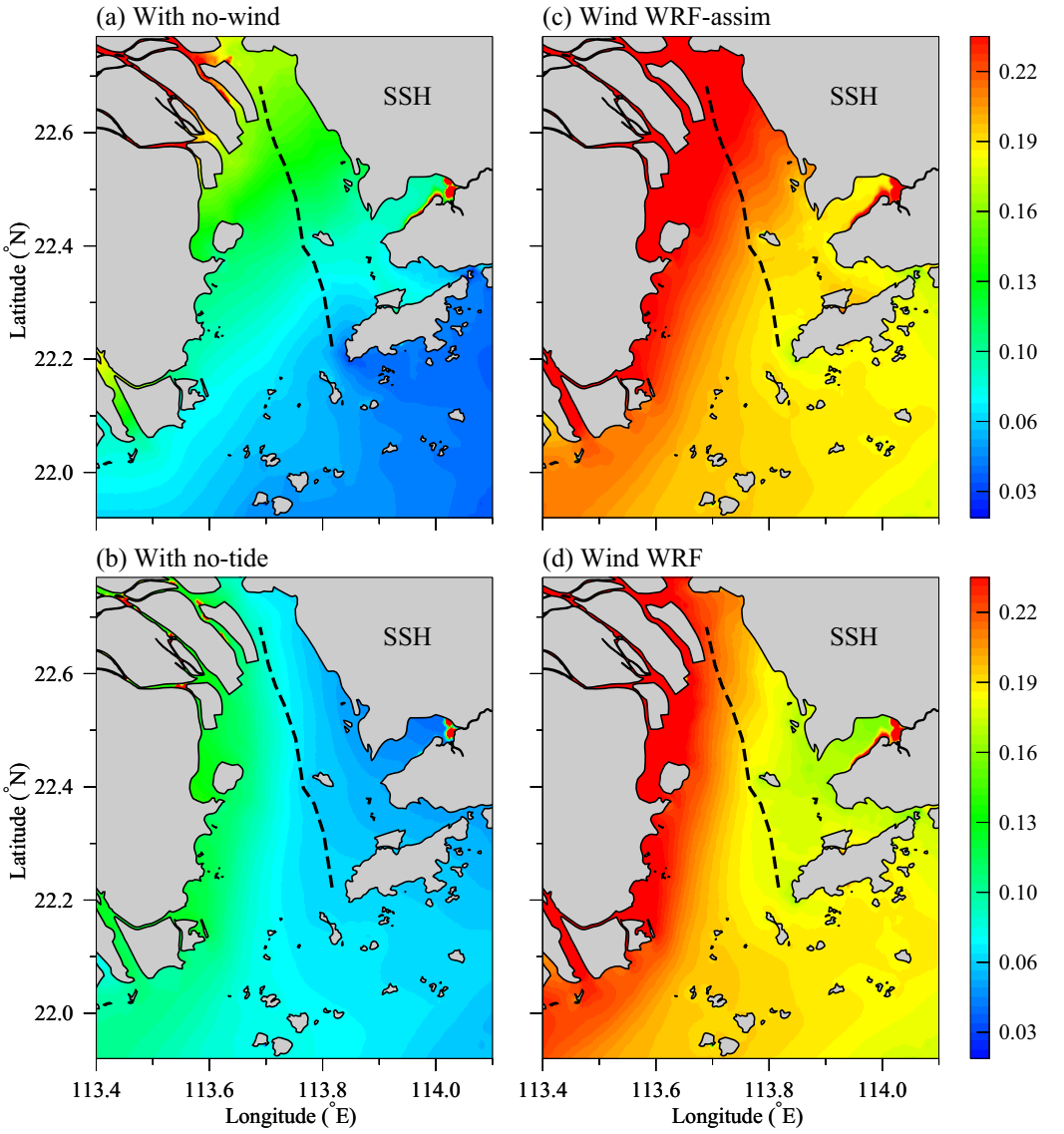

Figure 14. Monthly mean sea surface height in the (a) with no-wind, (b) with no-tide, (c) Wind WRF-assim, and (d) Wind WRF cases, respectively. The location of the transect S2 along the deep channel is indicated.

To understand the physical processes in more details, the mean subtidal sea surface height (SSH) was examined in Figure 14. It showed that there were three components of the SSH over the PRE which were caused by freshwater discharge, tides, and the winds, respectively. In case (a) with no wind, the combination of the freshwater discharge and tides resulted in a gravitational circulation with higher SSH located at the head of the estuary setting up a pressure gradient force to push the plume seaward. The components of the SSH due to the effect of winds in the cases with (c) Wind WRF-assim and (d) Wind WRF then could be derived by calculating the difference of those results obtained from case (a).

As displayed in Figures 15b and 15c, the results showed that the downwelling-favorable wind caused a pattern of the estuarine SSH which was generally opposite to that of the gravitational circulation with a center of low SSH located at the estuary head extending seaward in the direction of the winds and being embraced by higher SSH in the surrounding area. This wind-induced SSH may drive an estuary-shelf exchange with landward currents intruding upstream at the bottom and carrying the high salinity water into the PRE. To see this wind-induced SSH effect, an along-estuary transect S2 was chosen, which ran from the estuary mouth to the estuary head following the deep channel (Figure 1). By comparing the results in Figures 15d, 15f, and 15g, it was evident that when the wind forcing was turned on, the along-estuary

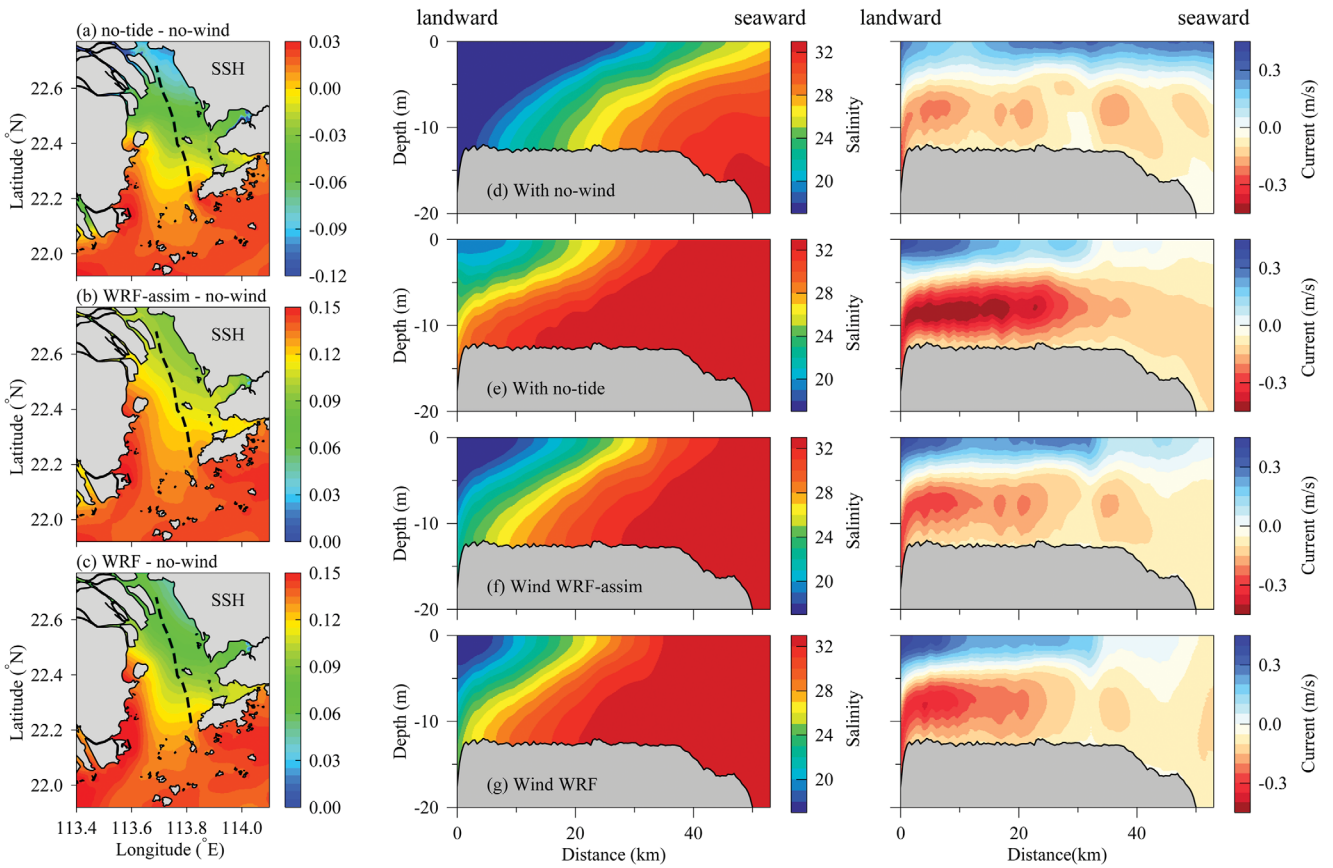

Figure 15. (left) Mean SSH in the case (a) no-tide: no-wind, (b) Wind WRF-assim: no-wind, and (c) Wind WRF: – no-wind, respectively. Please note that although the color range is different among the three cases, the absolute difference is the same so that the SSH gradients in the three cases are still comparable. (right) Mean salinity and currents along transect S2 in the (d) with no-wind, (e) with no-tide, (f) Wind WRF-assim, and (g) Wind WRF cases, respectively.

salinity contours significantly moved upstream under a stronger subsurface landward current. If comparing the upstream movement of the along-estuary salinity distributions with enhanced SSH gradients between the cases with Wind WRF-assim and Wind WRF, one could find that those changes occurred coincidently with the increase in wind speed. Therefore, the estuarine SSH produced by the remote influence of the regional-scale downwelling-favorable winds should drive an active estuary-shelf exchange through the sections at (3) and (4) (Figure 13). The intruded shelf water then had to be raised up at the center of the low SSH where it mixed with the discharged riverine water and to form the river plume with an enhanced transport as demonstrated in Figure 13. With this analysis, it is clear that the estuarine SSH set up by the downwelling-favorable wind represented the key physical mechanism to control the plume dynamics remotely.

To qualify the effect of tides on the plume dynamics through the estuarine SSH, the SSH in the case with no wind was subtracted from the SSH in the case with no tide in Figure 14 and the result is shown in Figure 15a to compare with the results in Figure 15b. It showed that with the same downwelling wind, the removal of the tidal effects caused an even stronger SSH gradient. Associated with that, the along-estuary salinity contours shifted farther toward the estuary head with the help of a significantly strengthened subsurface landward current (Figures 15e and 15f). By comparing the results in Figures 13–15 among all cases, it was evident that the case with no-tide had the strongest SSH gradient. Therefore, it caused the longest distance of the upstream intrusion of the salinity contours under the strongest subsurface landward current. As a result, there was the largest volume of the plume transport through section (2). This result clearly demonstrates that the role of tides on the plume dynamics is important not only locally but also remotely. This finding is consistent with previous studies, which show that the tidally induced turbulent mixing is an

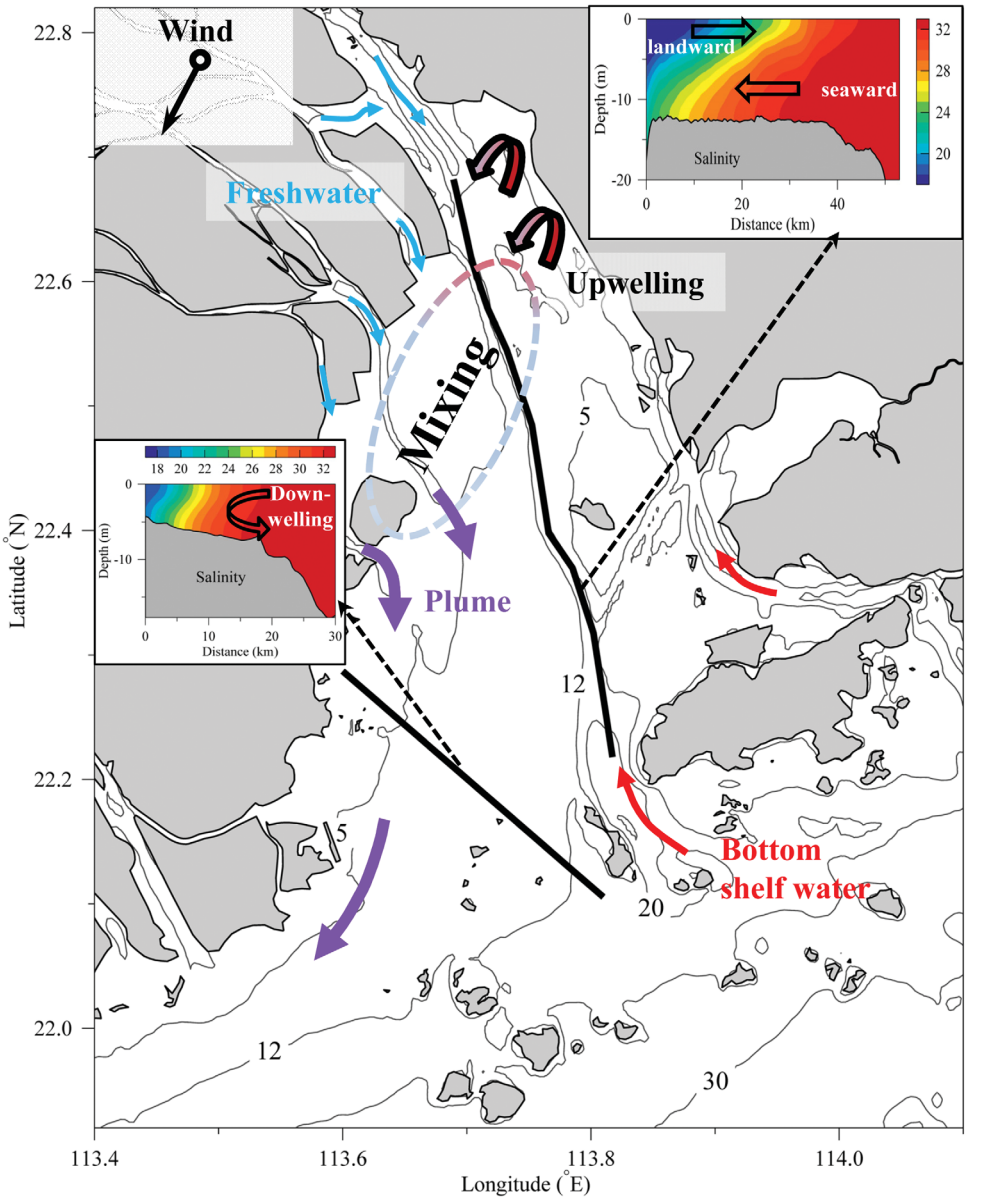

Figure 16. Schematic plot of the PRE plume dynamics under downwelling wind during the dry season.

important term in the estuarine dynamics [*Hansen and Rattray*, 1965; *Csanady*, 1973]. So, tides could affect the estuarine circulation and then influence the plume dynamics remotely.

5. Conclusions

Estuarine plume dynamics under a downwelling-favorable wind condition were examined in the Pearl River estuary using the PRE primitive-equation Finite-Volume Community Ocean Model (PRE-FVCOM). The numerical study was conducted in an estuarine environment with strong tidal influences and active wind-induced estuary-shelf exchange. These processes caused the plume to behave under more complex physics that has not been well addressed in previous studies.

According to the model results, we have summarized the plume dynamics under the downwelling-favorable winds with the local and remote influences of tides and winds (Figure 16). Specifically, the local effects of the downwelling-favorable winds on the plumes were similar to the theoretical descriptions of

coastal plumes which narrow the plume width and enhance the plume transport by setting up a vertically uniform downstream current at the plume edge. The inclusion of tides tended to weaken the effect of wind in the plume. Specifically, the effect of tides on the plume geometry was through turbulent mixing, which resulted in an adjustment of the isohalines in the plume. Besides that, the effect of the tides on the plume current was to enhance the buoyancy input from the upstream region which suppressed the local wind-induced mixing and weakened the vertically uniform downstream current. Effects of these local tides and winds on the plume mainly occurred on the offshore side of the front. On the inshore side of the front, the wind effects on the cross-shore momentum balance were canceled out by each other and the plume remained geostrophic with an offshore distance determined by the internal Rossby radius of deformation.

Finally, the estuarine sea surface elevation set up by the downwelling-favorable wind represents the remote controlling mechanism of the plume dynamics in the PRE. It drove an estuarine circulation with an active estuary-shelf exchange into the interior of the estuary. The intruded high-salinity shelf water was mixed with the discharged riverine water at the head of the estuary to form the plume and significantly enhance the plume transport. Again, tides can be involved in this process because the tidally induced turbulent mixing was an important term in the momentum balance of the estuarine circulation. As a result, tides can remotely influence the plume dynamics by weakening the estuarine circulation.

Acknowledgments

This research work was supported by the National Natural Science Foundation of China (grant 41206005), the Ocean Public Welfare Scientific Research Project, State Oceanic Administration of the People's Republic of China (grant 201305019-3), the Special Program for Applied Research on Super Computation of the NSFC-Guangdong Joint Fund (the second phase), and the CAS Strategic Pilot Science and Technology (XDA11020205). Changsheng Chen's participation was supported by the International Center for Marine Studies, Shanghai Ocean University. We would like to thank the National Supercomputer Center in Guangzhou and the Network and Information Technology Center at Sun Yat-sen University for providing the computing resources. The model data used in the paper are accessible by contacting the authors through the email address laizhig@mail.sysu.edu.cn and describing the purpose of usage. The observation data were collected from the 908 Ocean Survey Project which has to be accessed through the Project's public office.

References

Beardsley, R. C., and L. K. Rosenfeld (1983), Introduction to the CODE-1 moored array and large-scale data report, in *CODE-1: Moored Array and Large-Scale Data Report*, *Woods Hole Oceanogr. Inst. Tech. Rep. WHOI-83-23*, *CODE Tech. Rep. 21*, edited by L. K. Rosenfeld, pp. 1–16, WHOI, Woods Hole, Mass.

Blanton, J. O. (1981), Ocean currents along a nearshore frontal zone on the continental shelf of the southeastern United States, *J. Phys. Oceanogr.*, *11*, 1627–1637.

Chao, S. Y. (1988), Wind-driven motion of estuarine plumes, *J. Phys. Oceanogr.*, *18*(8), 1144–1166.

Chapman, D. C., and S. J. Lentz (1994), Trapping of a coastal density front by the bottom boundary layer, *J. Phys. Oceanogr.*, *24*, 1464–1479.

Chen, C. (2000), A modeling study of episodic cross-frontal water transports over the inner shelf of the South Atlantic Bight, *J. Phys. Oceanogr.*, *30*, 1722–1742.

Chen, C., L. Zheng, and J. Blanton (1999), Physical processes controlling the formation, evolution, and perturbation of the low-salinity front in the inner shelf off the Southeastern U.S.: A modeling study, *J. Geophys. Res.*, *104*, 1259–1288.

Chen, C., H. Liu, and R. C. Beardsley (2003), An unstructured, finite-volume, three-dimensional, primitive equation ocean model: Application to coastal ocean and estuaries, *J. Atmos. Oceanic. Technol.*, *20*, 159–186, doi:10.1175/1520-0426.

Chen, C., R. C. Beardsley and G. Cowles (2006a), An unstructured grid, finite-volume coastal ocean model (FVCOM) system, *Oceanography*, *19*, 78–89, doi:10.5670/oceanog.2006.92.

Chen, C., R. C. Beardsley, and G. Cowles (2006b), *An Unstructured Grid, Finite-Volume Coastal Ocean Model-FVCOM User Manual, 2nd ed., SMAST/UMASSD Tech. Rep. 06-0602*, Univ. of Mass.-Dartmouth, New Bedford, 318 pp.

Chen, C., et al. (2013), *An Unstructured-Grid, Finite-Volume Community Ocean Model FVCOM User Manual*, 3rd ed., *SMAST/UMASSD Tech. Rep. 13-0701*, Univ. of Mass.-Dartmouth, New Bedford, 404 pp.

Chen, C., G. Gao, Y. Zhang, Robert C. Beardsley, Z. Lai, J. Qi, and H. Lin (2016), Circulation in the Arctic Ocean: Results from a high-resolution coupled ice-sea nested Global-FVCOM and Arctic-FVCOM system, *Prog. Oceanogr.*, *141*, 60–80.

Choi, B. J., and J. L. Wilkin (2007), The effect of wind on the dispersal of the Hudson River plume, *J. Phys. Oceanogr.*, *37*(7), 1878–1897.

Csanady, G. T. (1973), Wind-induced barotropic motions in long lakes, *J. Phys. Oceanogr.*, *3*(4), 429–438.

Dai, M., X. Guo, W. Zhai, L. Yuan, B. Wang, L. Wang, P. Cai, T. Tang and W. Cai (2006), Oxygen depletion in the upper reach of the Pearl River estuary during a winter drought, *Mar. Chem.*, *102*(1), 159–169.

Ding, Y. (1994), *Monsoons Over China*, 419 pp., Kluwer Academic Publishers, Dordrecht, Boston.

Dong, L., J. Su, L. Wong, Z. Cao, and J. Chen (2004), Seasonal variation and dynamics of the Pearl River plume, *Cont. Shelf Res.*, *24*(16), 1761–1777.

Fong, D. A., and W. R. Geyer (2001), Response of a river plume during an upwelling favorable wind event, *J. Geophys. Res.*, *106*, 1067–1084.

Fong, D. A., W. R. Geyer and R. P. Signell (1997), The wind-forced response on a buoyant coastal current: Observations of the western Gulf of Maine plume, *J. Mar. Syst.*, *12*(1), 69–81.

Garcia Berdeal, I., B. M. Hickey, and M. Kawase (2002), Influence of wind stress and ambient flow on a high discharge river plume, *J. Geophys. Res.*, *107*(C9), 3130, doi:10.1029/2001JC000932.

Garvine, R. W. (2004), The vertical structure of the subtidal dynamics of the inner shelf off New Jersey, *J. Mar. Res.*, *62*, 337–371.

Gong, W., and J. Shen (2011), The response of salt intrusion to changes in river discharge and tidal mixing during the dry season in the Modaomen Estuary, China, *Cont. Shelf Res.*, *31*(7), 769–788.

Guo, X., and A. Valle-Levinson (2007), Tidal effects on estuarine circulation and outflow plume in the Chesapeake Bay, *Cont. Shelf Res.*, *27*(1), 20–42.

Hansen, D. V., and M. Rattray (1965), Gravitational circulation in straits and estuaries, *J. Mar. Res.*, *23*, 104–122.

Hetland, R. D. (2005), Relating river plume structure to vertical mixing, *J. Phys. Oceanogr.*, *35*(9), 1667–1688.

Hickey, B., S. Geier, N. Kachel, and A. MacFadyen (2005), A bi-directional river plume: The Columbia in summer, *Cont. Shelf Res.*, *25*(14), 1631–1656.

Houghton, R. W., C. E. Tilburg, R. W. Garvine and A. Fong (2004), Delaware River plume response to a strong upwelling-favorable wind event, *Geophys. Res. Lett.*, *31*, L07302, doi:10.1029/2003GL018988.

Hunter, E. J., R. J. Chant, J. L. Wilkin, and J. Kohut (2010), High-frequency forcing and subtidal response of the Hudson River plume, *J. Geophys. Res.*, *115*, C07012, doi:10.1029/2009JC005620.

Janzen, C. D., and K. C. Wong (2002), Wind-forced dynamics at the estuary-shelf interface of a large coastal plain estuary, *J. Geophys. Res.*, *107*(C10), 3138, doi:10.1029/2001JC000959.

Ji, X., J. Sheng, L. Tang, D. Liu, and X. Yang (2011), Process study of dry-season circulation in the Pearl River estuary and adjacent coastal waters using a triple-nested coastal circulation model, *Atmos. Ocean*, *49*(2), 138–162.
Jurisa, J. T., and R. Chant (2012), The coupled Hudson River estuarine-plume response to variable wind and river forcings, *Ocean Dyn.*, *62*(5), 771–784.
Lai, Z., R. Ma, G. Gao, C. Chen, and R. C. Beardsley (2015), Impact of multichannel river network on the plume dynamics in the Pearl River estuary, *J. Geophys. Res. Oceans*, *120*, 5766–5789, doi:10.1002/2014JC010490.
Lentz, S. (2004), The response of buoyant coastal plumes to upwelling-favorable winds, *J. Phys. Oceanogr.*, *34*(11), 2458–2469.
Lentz, S. J., and J. Largier (2006), The influence of wind forcing on the Chesapeake Bay buoyant coastal current, *J. Phys. Oceanogr.*, *36*(7), 1305–1316.
Li, M., and L. Zhong (2009), Flood-ebb and spring-neap variations of mixing, stratification and circulation in Chesapeake Bay, *Cont. Shelf Res.*, *29*(1), 4–14.
Liu, C., H. Xia, and D. Wang (2006), The observation and analysis of eastern Guangdong coastal downwelling in the winter of 2006, *Acta Oceanol. Sin.*, *32*(1), 1–9.
MacCready, P., and W. R. Geyer (2010), Advances in estuarine physics, *Annu. Rev. Mar. Sci.*, *2*, 35–58.
Mao, Q., P. Shi, K. Yin, J. Gan, and Y. Qi (2004), Tides and tidal currents in the Pearl River Estuary, *Cont. Shelf Res.*, *24*(16), 1797–1808.
Mazzini, P. L., J. A. Barth, R. K. Shearman, and A. Erofeev (2014), Buoyancy-driven coastal currents off Oregon during fall and winter, *J. Phys. Oceanogr.*, *44*(11), 2854–2876.
Moffat, C., and S. Lentz (2012), On the response of a buoyant plume to downwelling-favorable wind stress, *J. Phys. Oceanogr.*, *42*(7), 1083–1098.
Münchow, A., and R. W. Garvine (1993), Buoyancy and wind forcing of a coastal current, *J. Mar. Res.*, *51*(2), 293–322.
Pan, J., Y. Gu, and D. Wang (2014), Observations and numerical modeling of the Pearl River plume in summer season, *J. Geophys. Res. Oceans*, *119*, 2480–2500, doi:10.1002/2013JC009042.
Pawlowicz, R., R. C. Beardsley, and S. Lentz (2002), Classical tidal harmonic analysis with error analysis in MATLAB using T_TIDE, *Comput. Geosci.*, *28*, 929–937.
Pfeiffer-Herbert, A. S., C. R. Kincaid, D. L. Bergondo, and R. A. Pockalny (2015), Dynamics of wind-driven estuarine-shelf exchange in the Narragansett Bay estuary, *Cont. Shelf Res.*, *105*, 42–59.
Pimenta, F. M., and A. D. Kirwan (2014), The response of large outflows to wind forcing, *Cont. Shelf Res.*, *89*, 24–37.
Pritchard, D. W. (1956), The dynamic structure of a coastal plain estuary, *J. Mar. Res.*, *15*, 33–42.
Qiu, D., L. Huang, J. Zhang, and S. Lin (2010), Phytoplankton dynamics in and near the highly eutrophic Pearl River Estuary, South China Sea, *Cont. Shelf Res.*, *30*(2), 177–186.
Rennie, S. E., J. L. Largier, and S. J. Lentz (1999), Observations of a pulsed buoyancy current downstream of Chesapeake Bay, *J. Geophys. Res.*, *104*, 18,227–18,240.
Scully, M. E., C. Friedrichs, and J. Brubaker (2005), Control of estuarine stratification and mixing by wind-induced straining of the estuarine density field, *Estuaries*, *28*(3), 321–326.
Simpson, J. H., J. Brown, J. Matthews, and G. Allen (1990), Tidal straining, density currents, and stirring in the control of stratification, *Estuaries*, *13*, 125–132.
Warner, J. C., W. R. Geyer, and J. A. Lerczak (2005), Numerical modeling of an estuary: A comprehensive skill assessment, *J. Geophys. Res.*, *110*, C05001, doi:10.1029/2004JC002691.
Whitney, M. M., and R. W. Garvine (2005), Wind influence on a coastal buoyant outflow, *J. Geophys. Res.*, *110*, C03014, doi:10.1029/2003JC002261.
Winant, C. D. (2004), Three-dimensional wind-driven flow in an elongated, rotating basin, *J. Phys. Oceanogr.*, *34*(2), 462–476.
Wong, L., J. Chen, and L. Dong (2004), A model of the plume front of the Pearl River Estuary, China and adjacent coastal waters in the winter dry season, *Cont. Shelf Res.*, *24*(16), 1779–1795.
Yang, Z., and T. Khangaonkar (2009), Modeling tidal circulation and stratification in Skagit River estuary using an unstructured grid ocean model, *Ocean Modell.*, *28*(1), 34–49.
Zhao, H. (1990), *The Evolution of the Pearl River Estuary*, 357 pp., China Ocean Press, Beijing.
Zhang, W., H. Feng, J. Zheng, A. J. F. Hoitink, M. Van Der Vegt, Y. Zhu and H. Cai (2012), Numerical simulation and analysis of saltwater intrusion lengths in the Pearl River Delta, China, *J. Coastal Res.*, *29*(2), 372–382.
Zheng, S., W. Guan, S. Cai, X. Wei, and D. Huang (2014), A model study of the effects of river discharges and interannual variation of winds on the plume front in winter in Pearl River Estuary, *Cont. Shelf Res.*, *73*, 31–40.